

Yan Yan · Yifei Cui · Dingzhu Liu · Hui Tang · Yongjian Li · Xin Tian · Lei Zhang · Sheng Hu

Seismic signal characteristics and interpretation of the 2020 “6.17” Danba landslide dam failure hazard chain process

Abstract Landslide dam failures have devastating capability to cause significant hazards to human lives and infrastructure along their flooding paths. Recent studies have explored such hazards based on environmental seismology to analyze the process of evolution using the time-frequency characteristics of seismic signals. However, most research has focused on reconstructing individual processes (e.g., debris flows, landslides, and floods). Previous studies on a comprehensive analysis of the entire hazard chain process have been limited. Challenges lie in the integration of seismic signals with different energy levels during different hazard stages. To address this issue, post-hazard surveys, remote sensing, and seismic signals were obtained in this study to comprehensively analyze the evolution process of the Danba landslide dam failure hazard chain of June 17, 2020, in China. We developed weak-signal processing using a band-pass filter, empirical mode decomposition, fast Fourier transform, and short-time Fourier transform to process and analyze the seismic data and accurately extract the signals for the debris flow, landslide, flood, and noise attenuation in the hazard chain. The evolution process of each stage in the hazard chain was then interpreted. The debris flow, landslide, barrier lake bursting, and flood routing were analyzed to determine their evolution modes. In addition, the reactivation of ancient landslides downstream caused by flood erosion was also identified, with stage explanations. This method provides new ideas for interpreting the hazard chain processes and evolution modes of landslide dam failure hazard chains and theoretical guidance for future hazard early warning and mitigation.

Keywords Danba landslide dam failure · seismic signal · hazard chain interpretation · ancient landslide reactivation

Introduction

Rivers can form natural dammed lakes in response to debris flows or landslides that block the river valley and fill backwater into the upper river reaches (Yan et al. 2017; Li et al. 2020). Mountainous ravines and dense water systems are common in southwestern China, where dammed lakes pose a particularly high security risk (King et al. 1989; Huang et al. 2008; Wang et al. 2015; Wei et al. 2020). Debris flows can block the nearby river system under various environmental loads (Ding et al. 2020) to form a hazard chain as follows: debris flow → river blocking → landslide dam → outburst flood (Xu et al. 2009; Nian et al. 2018). Landslide dam failure is one of the important links of this hazard chain pattern and can be complex and devastating. Landslide dam failures are a serious threat to downstream communities and infrastructure (Cui et al. 2003; Sassa et al. 2005; Feng et al. 2020) and have caused significant damage in recent decades (Costa and Schuster 1988; Ermini and Casagli 2010; Feng 2012; Chen et al. 2020). Understanding the formation of landslide dam failure hazard chains and

evolution characteristics of each hazard stage is therefore of great significance for effective hazard mitigation.

Despite physical flume modellings and laboratory soil tests conducted to understand the evolution characteristics of each hazard stage (Begam et al. 2018; Zhou et al. 2019; Liu et al. 2020; Shi and Zhao 2020; Shi et al. 2021), in-depth research on landslide dam failure hazard chain is still hindered by comparison with real-time monitoring data (Fan et al. 2014; Carlo et al. 2015; Dal Sasso et al. 2014). Landslide dam failure hazard chains have attracted extensive attention in recent years (Cui et al. 2009; Niu et al. 2012; Zhou et al. 2013; Shi et al. 2015); however, because of limited on-site monitoring data, previous studies have mainly focused on remote sensing and on-site investigation (Fan et al. 2012; Cui et al. 2013; Safran et al. 2015). Remote sensing technology and satellite images typically only roughly reflect the surface kinematics of hazard chains and cannot be used to characterize internal process dynamics (Wang 2013; Liu et al. 2021; Ma et al. 2021), and on-site surveys are often limited by the site environment. The entire hazard chain evolution process has not been systematically investigated. Traditional on-site monitoring instruments are difficult to deploy in a timely fashion because of the sudden nature of landslide dam failure chains. The high destructiveness of these events also typically damages on-site monitoring equipment, which makes it difficult to collect uninterrupted monitoring data (Feng et al. 2020; Yan et al. 2020a). A thorough study of the entire landslide dam failure chain process poses substantial challenges (Cui et al. 2019) and remains poorly understood. New research methods are therefore required to supplement the lack of on-site monitoring techniques.

Several studies have proposed the application of seismic signal analysis methods in the field of environmental seismology to systematically study landslide dam failure chains (Hibert et al. 2014; Schimmel and Hübl 2016; Feng et al. 2017). When a debris flow or landslide blocks a river, the dam will ultimately break and a flood will evolve, which releases a tremendous amount of energy and generates surface and/or underground seismic signals (Yamada et al. 2012; Feng et al. 2020) that can be quantitatively recorded by a nearby seismic network (Wang et al. 2020). The analysis of such signals provides valuable information regarding the formation and evolution of landslide dam failure hazard chains, as well as dynamic characteristics such as occurrence time, scale, movement, and energy changes (Feng 2012; Kao et al. 2012; Zhang et al. 2019). Seismic signals are therefore an important emerging method to study landslide dam failure hazard chains and several studies have been carried out using this approach in a wide range of related studies (Huang et al. 2008; Feng 2012; Zhu et al. 2016). The seismic signals generated by debris flows and floods can be divided into two parts: long-period and short-period signals. Both signal types represent the corresponding dynamic characteristics of nearby hazard events to a certain extent

(Li et al. 2017); however, short-period signals are more difficult to model because of their rapid attenuation with distance from the signal source (Huang et al. 2007; Zhang et al. 2019). The main purpose at present is therefore to invert long-period signals by obtaining the force-time function of the corresponding hazard event and quantitatively analyzing its kinematic parameters (Brodsky et al. 2003; Huang et al. 2007). Yan et al. (2017) conducted field experiments on the failure of dammed lakes using broadband seismographs to monitor the seismic signals generated during the dam collapse. The short-time Fourier transform (STFT) was used to obtain the time-frequency characteristics of the seismic signal and characteristics of each frequency band during failure. An explanation for the signal change of each frequency band and its relationship with the dam failure process was determined. Zhang et al. (2019) analyzed the seismic signal amplitude of the Baige landslide in Tibet; determined its occurrence time; analyzed the force-time function, spectrogram, and landslide site; and provided an in-depth discussion on the evolution process and behavior patterns of landslide events. However, seismic signal collection is inevitably affected by interference signals, which increases the degree of signal contamination (Yan et al. 2020b). Effective seismic signal identification and extraction have therefore become an important aspect of the study of hazard chains. To improve the analysis reliability and signal recognition, the most common processing method is to identify signals with higher energy in the frequency domain and manually remove interference signals (Helmstetter and Garambois 2010; Sheng et al. 2018). For example, Feng (2011) distinguished weak surface wave signals from noise signals using empirical mode decomposition (EMD) and obtained the time-frequency spectrum of seismic signals based on the Hilbert–Huang transform (HHT). Previous reports have shown that the 2.94- and 2.75-Hz spectral amplitude curves may help to identify the occurrence times of a dam failure and corresponding flood process (Feng 2012). Most studies in the literature were generally based on seismic signals to reconstruct or invert a single hazard event (e.g., debris flow, landslide, floods) (Yamada et al. 2013; Yan et al. 2020a) and a systematic analysis of the entire chain process using seismic signals has not yet implemented. The development of an effective method to investigate the entire landslide dam failure hazard chain process based on seismic signal characteristics is therefore required.

To address these issues, we studied the “6.17” Danba landslide dam failure that occurred in 2020 using seismic signal data recorded by nearby seismic stations. The main seismic signal parameters were effectively extracted and used to interpret the entire process and determine the landslide dam failure process’s characteristics. This study provides a new method to interpret and characterize the full process of the landslide dam failure chain using seismic signals.

Study area and data source

In the early morning of June 17, 2020, heavy rainfall triggered the formation of debris flows in Meilonggou Gully in Danba County, Sichuan Province, China. A portion of the debris flow accumulated at the gully mouth and another portion blocked the Xiaojinchuan River and formed a dammed lake. The natural dam ultimately failed and the subsequent flood eroded the base of an ancient landslide, which caused a collapse of its front edge (the Aniangzhai landslide).

Geologic and topographic conditions

The study area is located on the right bank of the Xiaojinchuan River in the Meilonggou Gully area of Banshanmen, Danba County, in the eastern part of Ganzi Tibetan Autonomous Prefecture in Sichuan, China. The study area includes Meilonggou debris flow, Aniangzhai landslide, and the dammed lake. The area is located on the southeastern edge of the Qinghai–Tibet Plateau, west of the Chengdu Plain on the western slope of the Qionglai Mountains. Danba County is located in the high mountains of the Minshan, and Qionglai ranges from a topographic perspective. The Dadu River runs through the entire territory from north to south, cutting high mountains into remarkable three-dimensional landforms, and is part of the alpine valleys of western Sichuan Province (Fig. 1).

Significant deep-cutting and lateral erosion have occurred in the rivers of this area because of phased uplift of the Earth’s crust, which has resulted in various degrees of damage to the plateau. The valleys in the eastern, middle, and northern parts of the valley are mostly V-shaped, whereas the northwest and southern valleys are relatively gentle and mostly U-shaped. The river valleys are densely concentrated, the water systems in the area are relatively developed, and the planar form presents a parallel extending dendritic shape. The regional topography and landforms demonstrate notable water-erosion characteristics along the valley division (Fig. 2). Danba County belongs to the Maowen–Danba anticline of the Longmenshan fold-thrust fault zone and the composite site of the Sichuan–Yunnan–north-trending structure and Xiaojin–Jintang arc structure (Bai et al. 2020; Dong et al. 2018). Strong tectonic movement has left this area with a series of parallel arranged linear folds, secondary folds superposed on top of folds at all levels, and the development of a multi-level fault system. The surface lithology is mainly Sinian metamorphic rocks and Quaternary sedimentary layers. Tertiary carbonaceous slate, silty slate, and a small amount of deep metamorphic rocks are also present in some areas, and the outcropping formations are subject to heavy erosion.

Hydrological and meteorological conditions

Danba County belongs to the Tibetan plateau monsoon climate (subtropical plateau monsoon climate), which is distributed in a vertical belt. The temperature difference between the mountain top and river valley is >24 °C. Rainfall in Danba County is typically light and concentrated, with an average annual rainfall of 600 mm that is unevenly distributed and varies by altitude.

Danba County entered the flood season in June 2020 with a sudden increase of precipitation. From June 1 to June 17, the accumulated rainfall in Danba County reached 107 mm, accounting for approximately 1/5 of the average annual rainfall. According to the County Meteorological Bureau, rainfall began at 23:40 on June 16. Heavy short-term rain was concentrated in Bawang Township, Banshanmen Town, Donggu Town, and Badi Township in Danba. The maximum rainfall reached 34.1 mm/h and the hourly precipitation within 3 h was as high as 61.7 mm, an intensity that occurs only once in approximately 50 years, according to the regional meteorological record (Fig. 3). A rainstorm occurred suddenly on June 17 with high intensity but short duration (~10 min). According to the County Meteorological Bureau, the continuously heavy rains caused the upstream water flow to rapidly converge and the runoff of large and small rivers in the county

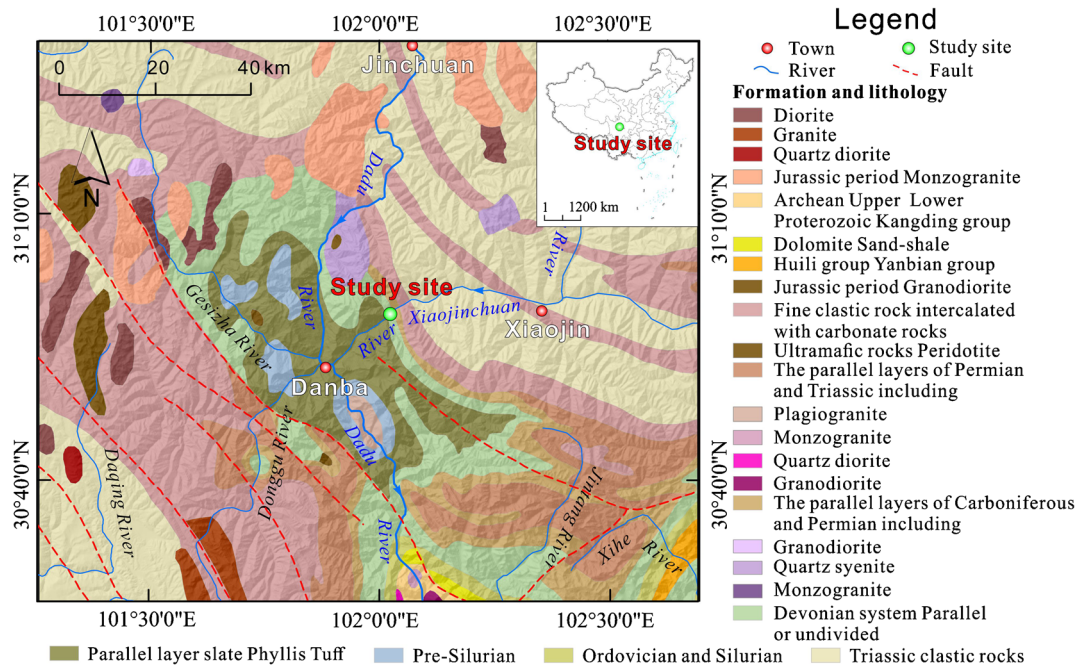


Fig. 1 Regional geological map of the study area

sharply increased. The floods along the large and small rivers and channels gradually formed strong hydrodynamic conditions, which washed the bank slopes along the gully and eroded and transported loose materials in the original channel.

Hazard chain

Meilonggou debris flow

Meilonggou Gully ($102^{\circ}1' 9.64''$ E, $30^{\circ} 59' 7.49''$ N) is located on the right bank of the Xiaojinchuan River in Banshanmen, Danba County. The main gully is approximately 10.7 km long and the drainage area is ~ 60 km². The highest point of the gully is ~ 4740 m, the lowest point is ~ 2130 m, and the relative elevation difference is ~ 2610 m. The average longitudinal slope is approximately 250‰ and the slope of the gully accumulation area is relatively gentle (Fig. 4a). The longitudinal gradient of the gully accumulation area section is approximately 80‰.

The continuous rainfall since June increased the groundwater content of the Xiaojinchuan River Basin, especially pore water in loose Quaternary sediments in Meilonggou Gully, which led to their destabilization. In the early morning of June 17, 61.7 mm of precipitation over a 3-h period caused a sharp increase in the surface runoff flow in the Xiaojinchuan River Basin. Surface water converged in the gully, which gathered in the Xiaojin River. Meilonggou Gully has a large catchment area and high mountain slopes, which makes it easy to form turbulent floods in the gully under the heavy short-term rainfall conditions. The flood in the gully drove the loose Quaternary sediments and bedrock on both sides of the spatula to form a highly destructive debris flow.

The material composition of the accumulated debris flow was mainly siliceous rock, slate, sandstone, crushed stone, and sandy soil. The overall sorting was poor (Fig. 4b). The gravel content was 30–40% with block sizes of 10–50 cm to as big as 3–5 m. Analysis of

the deposit characteristics and drainage basin of the debris flow indicates the Meilonggou debris flow was likely a sparse valley-type debris flow triggered by heavy rain.

Debris flow blocks the river to form a dammed lake

Debris flow accumulated at the mouth of the Meilonggou Gully because of the reduced slope. The accumulation area was $\sim 70,000$ m², the pile height was 2–3 m, the amount of washed out solid matter was $\sim 240,000$ m³, and the remaining accumulated volume at the gully was $\sim 110,000$ m³. The average height and width of the accumulated solid matter within 100 m from the gully mouth were ~ 30 and ~ 100 m, respectively. Approximately 130,000 m³ of solid matter entered the main river channel and formed a dammed lake with a length and width of ~ 200 and 50–100 m, respectively. These data and information are collected from the field survey conducted by the researchers of Sichuan Institute of Land and Space Ecological Restoration and Geological Hazard Prevention. The height of the accumulation area and the volume of the solid matter are calculated from the DEM data before and after the event. At the same time, it is corrected according to the in-field measurement. The Xiaojinchuan River was blocked and a dammed lake formed, causing the Meilonggou Gully channel and Xiaojinchuan River to rise by 8–12 m. The dammed lake extended to the Guanzhou Hydropower station dam, submerging a large number of houses in Guanzhou Village and causing 28 villager casualties.

Dam breach and outbreak flood

The thickness and firmness of the dammed lake accumulation body decreased gradually from the right bank to the left bank, which allowed the dammed lake water to easily overflow from the left bank and break. The overflow and natural outbreak actually diverted the Xiaojinchuan River by approximately 20 m to the left bank. The outburst current continued to wash away an ancient landslide on the right bank (Fig. 4c).

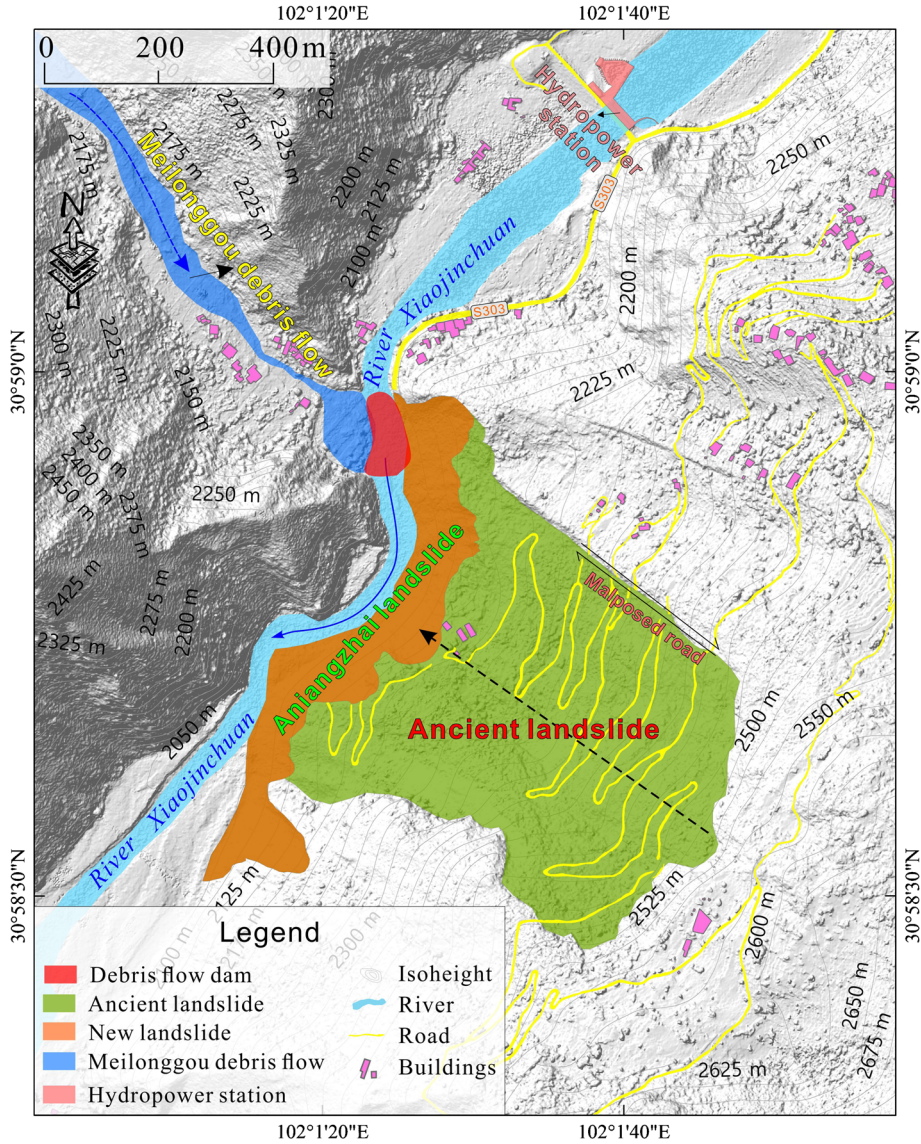


Fig. 2 Topographic map of the study area (The study area includes Meilonggou debris flow, Aniangzhai landslide, and the dammed lake.)

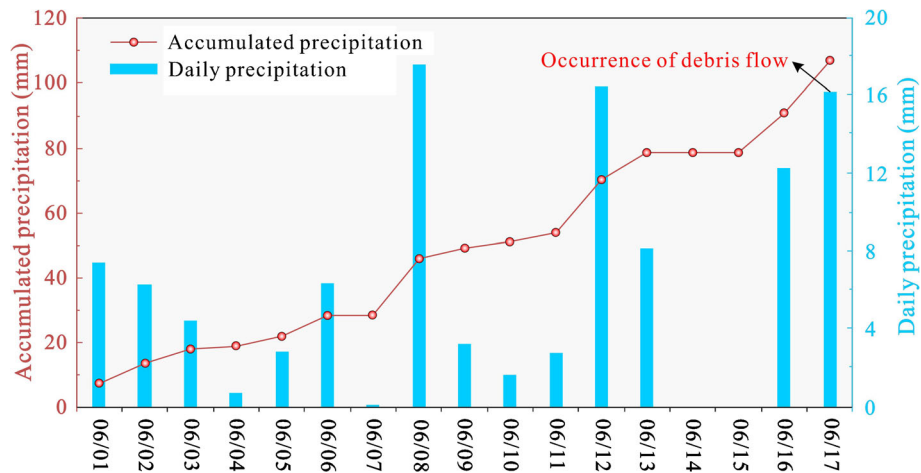


Fig. 3 Rainfall data of Danba County from June 1 to June 17, 2020 (The rainfall station (101° 31' 48" E, 30° 31' 48" N) closest to the study area is located in Danba County, which is 17 km southwest from the study area.)

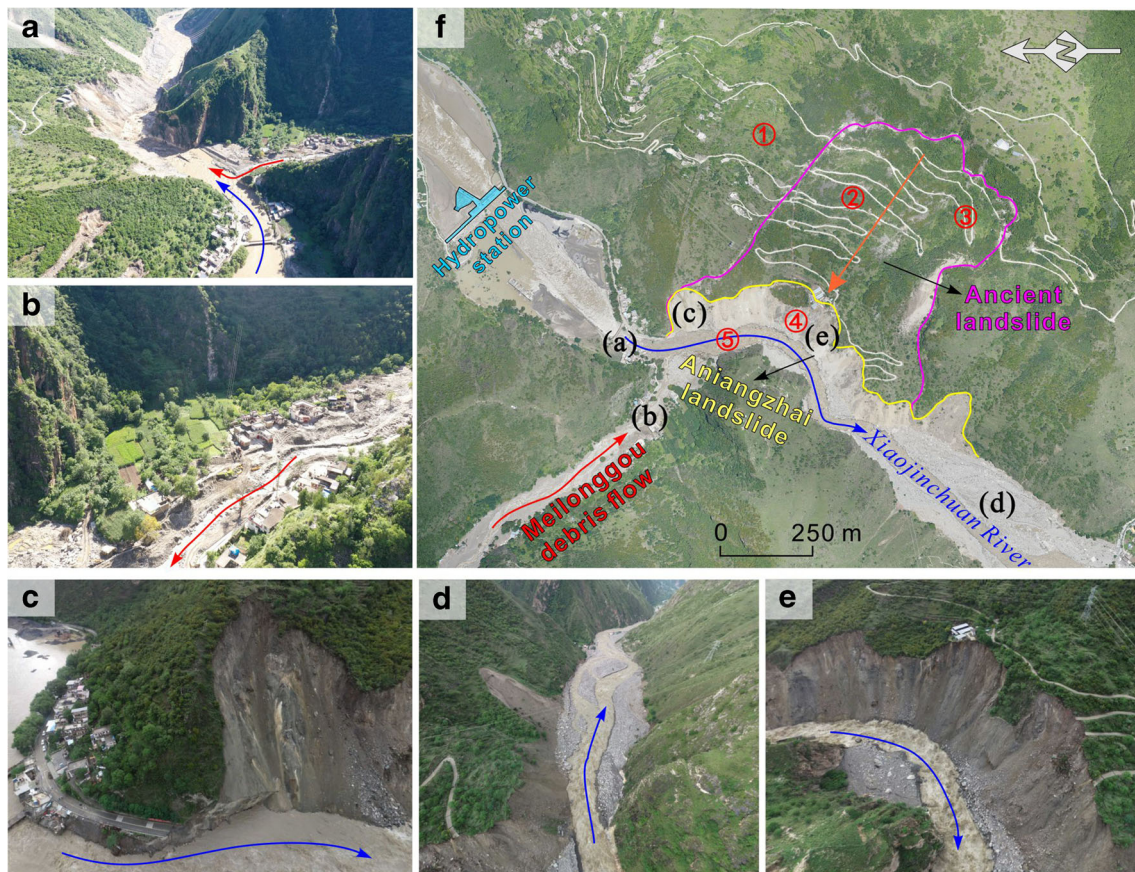


Fig. 4 Site photos of the hazard chain process of the Danba dammed lake. **a** Relative spatial relationship between the Aniangzhai ancient landslide accumulation body, Meilonggou Gully, and the Xiaojinchuan River. This is an overhead photo at point a in panel f. **b** Photograph after the Meilonggou debris flow. **c** After the first failure of the dammed lake. The surface formed by the collapse of the Aniangzhai landslide and represents the photo at point c in panel f. **d** Photograph of the lower reaches of the Xiaojinchuan River after the Aniangzhai landslide (point d in panel f). **e** Photograph of the flood after the second outbreak of the dammed lake caused by the Aniangzhai landslide. **f** Remote sensing image of the resurrection area of the ancient landslide: ① upstream rift zone of the resurrected body; ② middle activity zone of the resurrected body; ③ teardown zone downstream of the resurrected body; ④ landslide area at the front edge of the ancient landslide and landslide area of the most current landslide; and ⑤ accumulation of the Aniangzhai landslide area and dam body area of the landslide dam

Reactivation of the Aniangzhai ancient landslide

An ancient landslide ($102^{\circ} 1' 36.37''$ E, $30^{\circ} 58' 42.39''$ N) has been found close to Aniangzhai Village on the left bank of the Xiaojinchuan River with an area of ~ 1.4 km² and average thickness of ~ 50 m (Fig. 4f). The last large-scale slide of this ancient landslide occurred ~ 120 years ago, which led to its overall decline and spread into a “fan-shaped” plane. The trailing edge of the ancient landslide had a steep wall controlled by rock formations with a slope of $60\text{--}70^{\circ}$, elevation of 2850 m, relative elevation difference of ~ 818 m, and average thickness of ~ 50 m. The internal terrain of the landslide was relatively gentle with a slope of $35\text{--}45^{\circ}$. The front edge of the ancient landslide was a gentle slope platform formed by ancient landslide deposits.

The landslide area mainly consisted of the gentle slope platform on the front edge of the ancient landslide, with a total length of ~ 500 m and height of ~ 60 m. The landslide area was ~ 0.3 km² with a volume of ~ 6 million m³. There was a 60-m open surface upstream of the landslide area. This open surface produced traction-based sliding, which triggered the collapse of the front edge of the ancient landslide to form the most recent Aniangzhai landslide. The Aniangzhai landslide experienced

multiple landslide events that accumulated in the river to form a dammed lake. The landslide surface was relatively steep. The material composition of the landslides was the deposits of the ancient landslide front edge (Fig. 4d), which were mainly gravel and mud. The lithology of the rubble was phyllite and quartzite with diameters of mostly 25–35 cm but also reaching up to 8.0 m. The diameter of the gravel was mainly 3–10 cm and boulders were locally observed. With coarse particles as the framework, the pores were filled with gray-yellow silt to form a compact structure and moderate degree of cementation. The dammed lake that formed after the loose accumulation body slid downward was easily broken, and a flood peak occurred that caused several flood hazards downstream (Fig. 4e). The landslide dam failure caused by the landslides and debris flow notably caused cumulative damage that affected 12 townships, 112 villages, 5036 households, and 20,896 people in Danba County.

The Aniangzhai landslide partially resurrected an area of ~ 0.62 m² in the middle and front parts of the ancient landslide. The resurrected area was in the shape of a trapezoid with a maximum horizontal displacement of 10.2 m and maximum vertical displacement of 5.5 m. The entire resurrected body of

the ancient landslide was deformed at a constant velocity (Fig. 4f). There were many fractures in the middle of the ancient landslide, and the landslide changed from traction-dominated to forward-pull and push-back (i.e., slip mode dominated by pushing).

Ground motion records and signals

Approximately 33 seismic stations deployed by the China Earthquake Administration in Sichuan and Qinghai provinces are located within 200 km of the study area (Fig. 5). Based on the hazard occurrence time obtained from a survey of residents near Meilonggou Gully and Aniangzhai, we processed and screened the seismic signals recorded by these 33 stations from 19:00 on June 16 until 19:00 on June 17 (local time, UTC+8). The seismic signal characteristics were used to interpret the hazard chain process in this case.

Methodology

The relatively low-energy seismic signal and relatively strong absorption and attenuation make the seismic signal of this hazard event recorded by each station relatively weak and challenging to identify. We therefore designed weak-signal processing and analysis procedures (Fig. 6). A low-pass filter, EMD, STFT, and other methods were used to process and analyze the seismic signal data recorded by the seismic stations and extract the signal data and noise attenuation of each stage of the hazard chain (Yan et al. 2020b).

Low-pass filter (LP filter)

By passing frequencies within a certain range with low-pass filters, the hazards-related seismic signals are obtained in a specific frequency band. The cut-off frequency of the low-pass filter is 0.1 Hz.

Empirical mode decomposition (EMD)

EMD can adaptively decompose nonstationary and nonlinear signals into a set of orthogonal components, separate the main characteristic component from the remaining components, and obtain a clear time-domain curve, thereby achieving noise reduction of seismic signals (Feng 2011; Lei et al. 2018). The signal is decomposed into a set of orthogonal components, named as intrinsic mode functions (IMFs). In this study, EMD is used to decompose into 15 IMF components, and then IMF1~IMF4 components are filtered out. In general, any signal $x(t)$ can be decomposed by the EMD process according to the Eq. (1) (Huang and Wu 2008):

$$x(t) = \sum_{i=1}^n IMF_i(t) + r_n(t) \quad (1)$$

where n is the number of modes.

Fast Fourier transform (FFT)

FFT can obtain the frequency spectrum of the signal and analyze the available frequency changes with time, the time when each component appears, and the instantaneous frequency and its amplitude at each moment (Yan et al. 2017, 2019, 2020a).

Short-time Fourier transform (STFT)

STFT can obtain the frequency domain information of the signal while retaining the time domain distribution information of the signal (Yan et al. 2017, 2019, 2020b). A time-frequency localized window function is here applied to the analyzed discrete time series $x(t)$. $x[n]win[n]$ is a stationary signal within different finite time windows; thus, the power spectra can be calculated from Eq. 2. The window length of STFT transformation is 2^{15} (32768). $nfft$ is the number of DFT points, and it was usually given a value of 2^P , where $P = \lceil \log_2 N_w \rceil$. The $\lceil \cdot \rceil$ symbols denote the ceiling function and N_w refers to the window length. In this study, $N_w = 32768$. Thus, $nfft = 2^{\lceil \log_2(32768) \rceil} = 32768$.

$$stft\{x(t)\}(m, \omega) = X(m, \omega) = \sum_{n=-\infty}^{\infty} x[n]\omega[n-m]e^{-j\omega n} \quad (2)$$

where m is the window start time and ω is the angular frequency $\omega = 2\pi f$ for frequency f .

Results and analysis

Seismic signal characteristics of the hazard stages and processes

Although the scales of the debris flow and landslide were relatively small, the seismic stations of the nearby China Seismic Network recorded a certain degree of signals caused by the debris flow, outbreak flood, flood evolution, and landslide. According to the time-frequency domain signal of various geological hazards shown in Table 1, the seismic records from stations within about 130 km from the Aniangzhai landslide on June 17–20 were analyzed and selected. We examined 6 stations within radius 130 km from the study area for all hazards chain, i.e., Meilonggou debris flow, Aniangzhai landslide, and dammed lake-outbreak flood, and resulting XJI station that showed a strong effective signal as we have shown in Table 2. The Aniangzhai landslide and dammed lake-outbreak flood recorded at the XJI station generated the strongest energy and highest signal-to-noise ratio. We therefore mainly used the XJI station data in the subsequent analysis of the signal characteristics of the three events.

Debris flow

Of the 33 stations, only the XJI station, which is relatively close to Meilonggou Gully (34 km), effectively recorded seismicity caused by the Meilonggou debris flow. The signal-to-noise ratio of the DFU station slightly farther away was low and therefore impossible identifies an effective debris flow seismic signal. The debris flow signal of Meilonggou was relatively strong in the horizontal direction and the energy in the vertical direction was weak; thus, the event characteristics were not clearly identified. In the horizontal direction, the signal-to-noise ratio of the seismic signal in the east–west direction was higher than that in the north–south direction, which is the same as the extension direction of Meilonggou. This is approximately consistent with the west-to-east characteristics: namely, the evolution of debris coming from northwest to the southeast as shown in Fig. 2. From the perspective of the signal amplitude energy, the seismic amplitude in the east–west direction was approximately six times higher than that in the north–south direction and approximately four times higher than

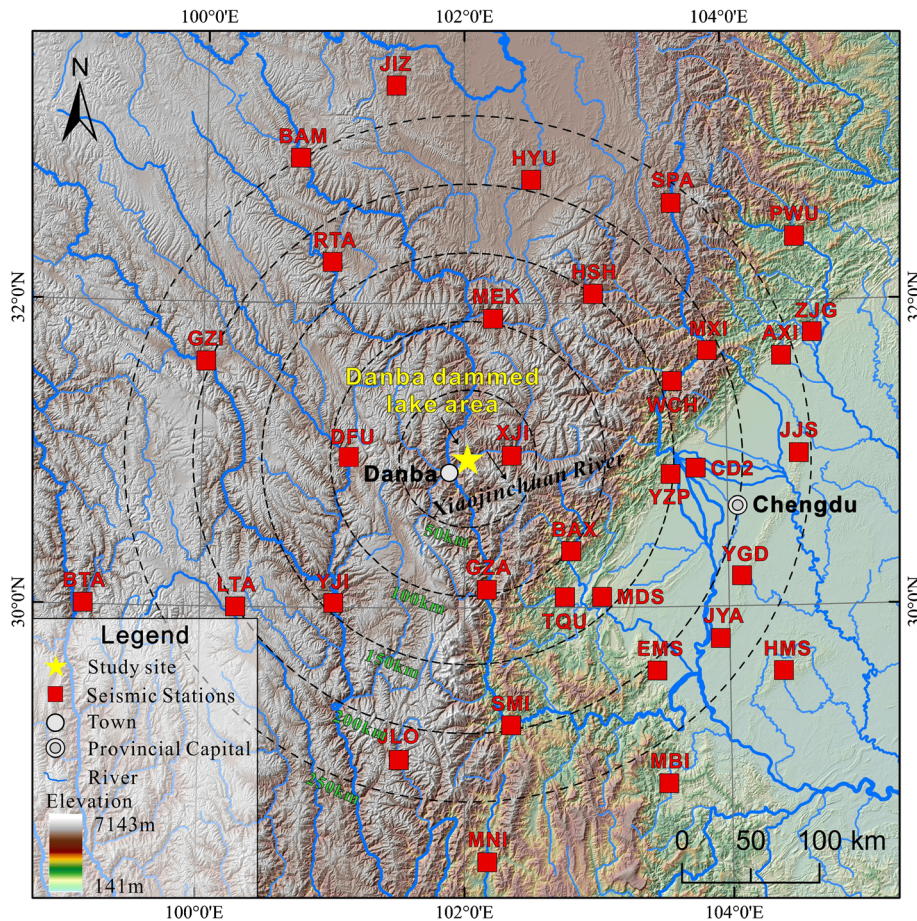


Fig. 5 Schematic diagram of the relative position relationship between the seismic station and study area

the vertical direction. The east–west seismic signal had the strongest energy amplitude and highest signal-to-noise ratio.

The seismic signal frequency of the Meilonggou debris flow was low with an effective signal frequency of <0.1 Hz and environmental noise frequency of $0.06\text{--}0.08$ Hz. The signal-to-noise ratio in the east–west direction was high and the time-frequency spectrum energy of background noise was weak; thus, the event was not clearly identified. The signal-to-noise ratio of the seismic signal in the north–south direction was slightly lower and the event was identified in the time spectrum, although its energy was relatively weak. The seismic signal in the vertical direction was extremely weak and the signal-to-noise ratio was less than 1, which made it impossible to identify an effective seismic signal. The time spectrum reflects the background noise characteristics and shows irregularly shape feature bands in the range of $0.06\text{--}0.08$ Hz (Fig. 7).

Due to the difference in the scale of different debris flows, the difference in seismic waveform and time-frequency characteristics is relatively large, and it is difficult to adopt a fixed amplitude difference and time-frequency range. In actual operation, it is often determined according to the relative magnitude of the amplitude. For example, the amplitude difference between the debris flow seismic signal and the background noise is about 10 times, and the frequency range is about 10 times the difference. So, the

judgment of the start and end time of a debris flow mainly depends on the difference between the energy in the time spectrum and the background energy. The seismic signal generated during the occurrence of the debris flow makes the energy of this stage significantly stronger than that of the non-debris flow. This feature is most obvious in the time-frequency spectrum. In the different stages of the debris flow, the movement speed of the debris flow and the scale of the debris flow are different. For example, the debris flow velocity in the initial start-up stage is small, and the debris flow velocity in the rapid evolution stage is large-scale, while the debris flow velocity in the accumulation stage decreases and the movement scale becomes smaller. The energy of the seismic signal is positively correlated with the speed and scale of the debris flow. Therefore, the debris flow is divided into stages according to the time domain amplitude and the energy of the time spectrum of the seismic signal (Tsai et al. 2012; Yan et al. 2017; Lai et al. 2018).

From the time-domain curve and time-frequency spectrum of the seismic signal in the east–west and north–south directions, the start and end times of the debris flow can be clearly identified at approximately 02:50 and 03:20 (local time) on June 17, 2020, respectively, lasting 30 minutes. From the time-domain curve and time spectrum of the debris flow, the Meilonggou debris flow can be divided into three stages. The signal of the first stage

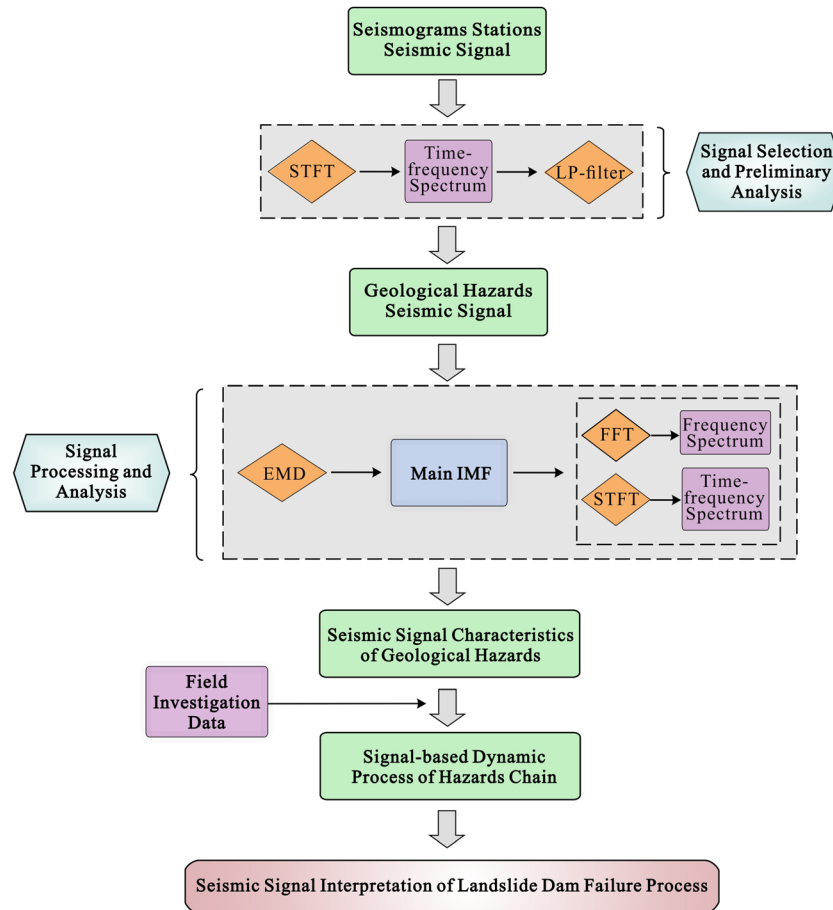


Fig. 6 Flow chart of the seismic signal analysis and processing method used in this study (STFT, short-time Fourier transform; LP filter, low-pass filter; EMD, empirical mode decomposition; IMF, intrinsic mode function; FFT, fast Fourier transform)

gradually increases, corresponding to the initiation stage of the debris flow. The second stage is characterized by strong amplitude, corresponding to the evolution stage of the debris flow. The third stage is a weak-amplitude stage, corresponding to the deposition stage.

Outbreak flood

The Xiaojinchuan River was later diverted 12 m to the left and flood discharge began. The discharge caused a sharp flow increase in the downstream river section below Aniangzhai. The seismic signals generated by the outbreak flood were recorded by seismic stations on both sides of the river. Five stations of the downstream section of the Xiaojinchuan River (east of Aniangzhai) clearly recorded the signal characteristics of the outbreak flood. The signal characteristics of the flood were typical broadband characteristics with a frequency range of 0–40 Hz. The frequency range in the east–west direction was relatively narrow (0–23 Hz), and that in the north–south and vertical directions was 0–30 Hz (Fig. 8). The three components were all band-shaped and had relatively strong amplitudes in the time domain without clear shapes. Analysis of the signals after 00:50 on June 17, 2020, showed that the initial outbreak of the dammed lake occurred at 6:37 on June 18 and a second outbreak occurred ~1 h later at 7:47.

Ancient landslide reactivation

Only three stations relatively close to Aniangzhai clearly recorded a signal of the landslide. The time-domain morphology of the seismic signals from the three stations all show spindle-shaped features. The XJI station recorded the highest signal-to-noise ratio with the most apparent spindle features, which can be identified as the beginning and end of the landslide. Similar to the debris flow signal characteristics of Meilonggou, the Aniangzhai landslide generated relatively strong horizontal signals and relatively weak vertical energy. The vertical component did not clearly indicate the landslide start and end time (Fig. 9). In the horizontal direction, the signal-to-noise ratio and amplitude energy of the seismic signal were higher in the east–west direction than in the north–south direction. This is consistent with the characteristics of the Aniangzhai landslide that the sliding direction was north–east and the landslide height difference was relatively small. From the perspective of signal amplitude energy level, the seismic amplitude in the east–west direction was approximately twice as large as that in the north–south direction, and the seismic amplitude in the south direction was approximately twice as large as in the vertical direction. From the signal amplitude, the seismic signal in the east–west direction showed the strongest energy and highest noise ratio.

Table 1 Seismic signal parameters of different types of geological hazard events

Types of geological hazard	Event/year	Duration (s)	Frequency range/Hz	Time domain feature	Time-frequency feature	Landslide volume/10 ⁴ m ³	Reference
Landslide	Tavanasa collapse /2002	40	1–10	Single spindle	Single peak	9	Dammeier et al. 2011
	Aiguille Dru collapse /2005	50	1–8	Double spindle	Double peak	15	Dammeier et al. 2015
	Laguna Beach landslide /2005	35	0–4	Double spindle	Double peak	26	Richter and Trigg 2008
	Monte Rosa collapse /2007	110	1–18	Single spindle	Single peak	30	Huggel 2009
	Shiaolin landslide /2009	80	0–3	Single spindle	Single peak	2500	Tsou et al. 2011
	Formazacollapse /2009	100	1–25	Single spindle	Single peak	70	Dammeier et al. 2015
	Preonzocollapse /2012	80	1–20	Single spindle	Single peak	21	Loew et al. 2017
	Xinmo landslide /2017	100	0–2	Double spindle	Double peak	1800	Yan et al. 2020a
	Piz Gengalo collapse /2017	130	1–20	Single spindle	Single peak	300	Amann et al. 2018
	Shuicheng landslide /2019	240	4.5–6	Double spindle	Double peak	100	Yan et al. 2020b
	Event/year	Main frequency/- Hz	Frequency range/Hz	Time domain feature	Time-frequency feature	-	Reference
Landslide dam failure	Tanwan landslide dam failure experiment /2017	10–45	0–50	Flat spindle+microseismic waves	Columnar+ energy of the end signal decreases and frequency bandwidth stable	-	Yan et al. 2017
	Dongchuan debris flow /2004	10–50	0–50	Flat Double spindle+microseismic waves	Peak +energy of the end signal decreases and frequency bandwidth stable	-	Hu et al. 2011
Debris flow	Illgrabenn debris flow /2008	3–20	1–20	Flat spindle+microseismic waves	Columnar +energy of the end signal decreases and frequency bandwidth narrows	-	Kogelnig et al. 2014
	Lattenbach debris flow /2008	5–20	0–50	Spindle+microseismic waves	Columnar +energy of the end signal decreases and frequency bandwidth narrows	-	Schimmel and Hübl 2016

Table 1 (continued)

Types of geological hazard	Event/year	Duration (s)	Frequency range/Hz	Time domain feature	Time-frequency feature	Landslide volume/ 10^4 m^3	Reference
	Luojiayu debris flow /2010	10–50	20–40	Spindle+microseismic waves	Peak +energy of the end signal decreases	-	Huang et al. 2020
	Marderello debris flow /2013	0–30	1–10	Spindle+microseismic waves	Peak +energy of the end signal decreases and frequency bandwidth narrows	-	Arattano et al. 2014

Similar to the large difference between the energy of the seismic signal generated by the debris flow and the energy of the background signal, we use the amplitude difference between the landslide seismic signal in the time domain and the background signal and the energy difference in the time spectrum to determine the start and end time of the landslide. The division of landslide stages is mainly based on two principles: (1) based on energy difference similar to the debris flow seismic signal, the energy and frequency width of the landslide stage is higher than the initial starting stage and the gradual stabilization stage; and (2) for normal landslide events, the seismic signal shows a spindle-shaped characteristic. That is, the signal amplitude gradually increases, and the frequency range gradually widens during the starting stage. As the landslide progresses, after the signal energy reaches the maximum and the frequency range reaches the maximum, the energy and frequency range begin to decrease. The initial stage of some landslides may be relatively fast, at this time the landslide signal presents a cone-shaped characteristic. Therefore, the landslide stage is determined according to this principle. The sliding stage of this landslide stage consists of multiple small landslides (Brodsky et al. 2003; Feng 2011; Yan et al. 2020a, 2020b).

Similar to the frequency characteristics of the Meilonggou debris flow seismic signal, the seismic signal of the Aniangzhai landslide also exhibited relatively low-frequency characteristics. The landslide signal frequency was <0.1 Hz and mainly concentrated in 0–0.02 Hz. The frequency of the environmental noise was approximately 0.06–0.08 Hz. The signal-to-noise ratio of the east–west component was high, the time-frequency spectrum energy of the background noise was weak, and the event characteristics were not clearly identified. The time-frequency spectrum reflects the landslide signal characteristics. The signal-to-noise ratio of the seismic signal in the north–south direction was slightly lower and the time spectrum characteristics were identified. The energy of the background noise was within the frequency band of 0.06–0.08 Hz. The energy of the vertical seismic signal was relatively weak with the lowest signal-to-noise ratio (~ 1.5). The background noise was 0.06–0.08 of the time spectrum and showed irregular band-like characteristics. The frequency of the vertical seismic signal was also relatively high, ranging from 0 to 0.1 Hz, and the energy mainly concentrated above 0.04 Hz.

From the time-domain curve and time-frequency spectra of the seismic signal in the east–west and north–south directions, the start and end times of the landslide are clearly identified at approximately 14:10 and 16:00, respectively, on June 17, 2020, lasting 110 min. The entire landslide signal can be decomposed into multiple cone-shaped signal features, corresponding to a continuous landslide composed of multiple consecutive landslides. From the time-domain curve and time-frequency spectrum of the landslide, the Aniangzhai landslide process can be divided into three stages. The signal of the first stage gradually increases, corresponding to the initiation stage. The second stage shows a strong amplitude, which corresponds to the continuous collapse. The third stage is the weak-amplitude stage, corresponding to the gradual stabilization stage.

Table 2 Statistical results of the seismic signal strength related to the landslide, debris flow, and outbreak flood recorded by seismic stations near the Aniangzhai landslide

Station	Distance to Danba dammed lake area (km)	Seismic signal strength of debris flow	Seismic signal strength of outbreak flood	Seismic signal strength of landslide
XJI	34	Strong	Strong	Strong
DFU	84	Slightly weak	Slightly weak	Slightly weak
TQU	126	N/A	Slightly weak	Extremely weak
GZA	99	N/A	Slightly weak	N/A
BAX	104	N/A	Slightly weak	Weak
MEK	102	N/A	Slightly weak	N/A

Signal-based hazard processes

Initiation-evolution-deposition process of debris flow

Heavy rainfall in the early morning of June 17 caused the surface water upstream of Meilonggou to flow into Meilonggou, and the flowing water in the gully gradually drove the gully deposits downward. Because of the relatively large ditch slope, the flowing water and gully deposits began to form a low-density debris flow due to gravity. The flow and density continued to increase as well as the ability to erode loose unstable sediments and weathered metamorphic rocks in and on both sides of the gully. The cyclic effect of these factors rapidly enlarged the scale of the debris flow, corresponding to the initiation stage. The seismic signal of this stage shows an increasing seismic amplitude trend, and the range and energy of the energy cluster from the time spectrum also simultaneously increase.

The debris flow gradually reached the carrying capacity limit related to the slope and shape of the Meilonggou Gully, and its ability to scour and scrape the weathered bedrock on both sides of the channel and bottom of the trench no longer increased. The seismic signal at this stage shows large-amplitude characteristics. The amplitude spectrum shows characteristics of the largest energy cluster width (highest frequency) and highest energy. This stage corresponds to the debris flow evolution in the middle and lower reaches of Meilonggou.

The characteristics of the rapid deposition of the debris flow are clearly reflected in the seismic signal. The signal shows a sudden change from the evolution stage to the deposition stage. After the evolution stage, the signal-to-noise ratio is close to 1. From the time-frequency spectrum, the energy in the frequency band (0–0.004 Hz) of the seismic signal in the deposition stage is roughly equal to the energy in the background signal frequency band (0.06–0.008 Hz).

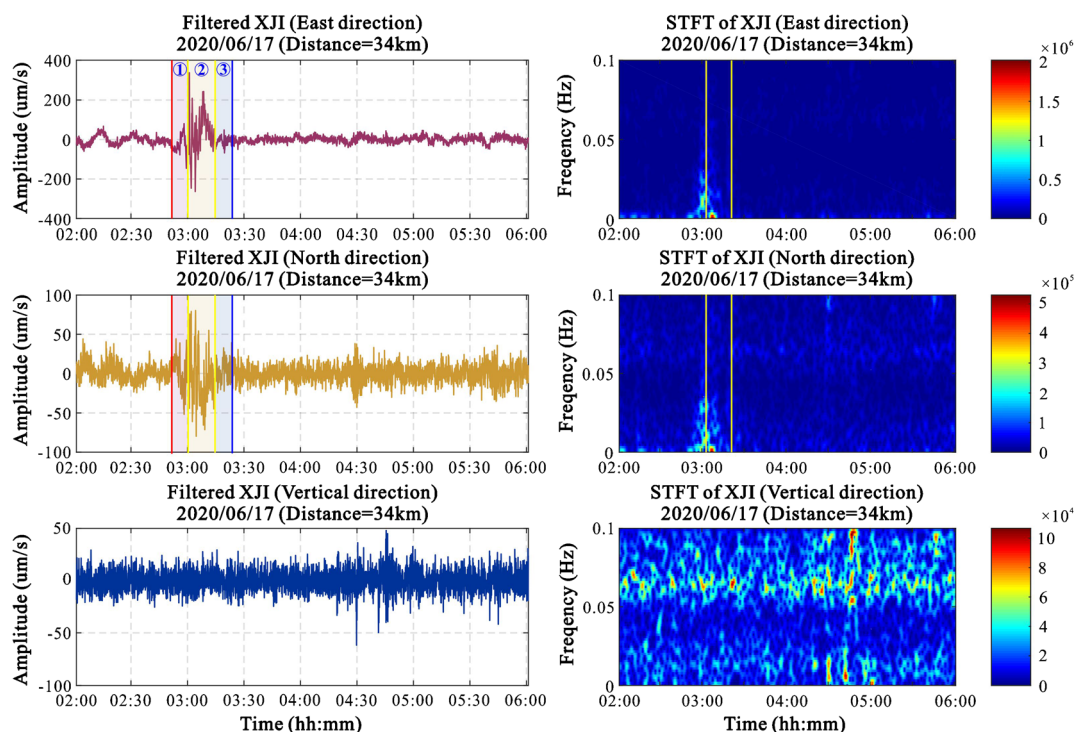


Fig. 7 Time domain seismic signal and time-frequency characteristic curve of the Meilonggou debris flow: ① initiation stage; ② evolution stage; and ③ deposition stage. The red and blue lines represent the start and end times of the debris flow, respectively

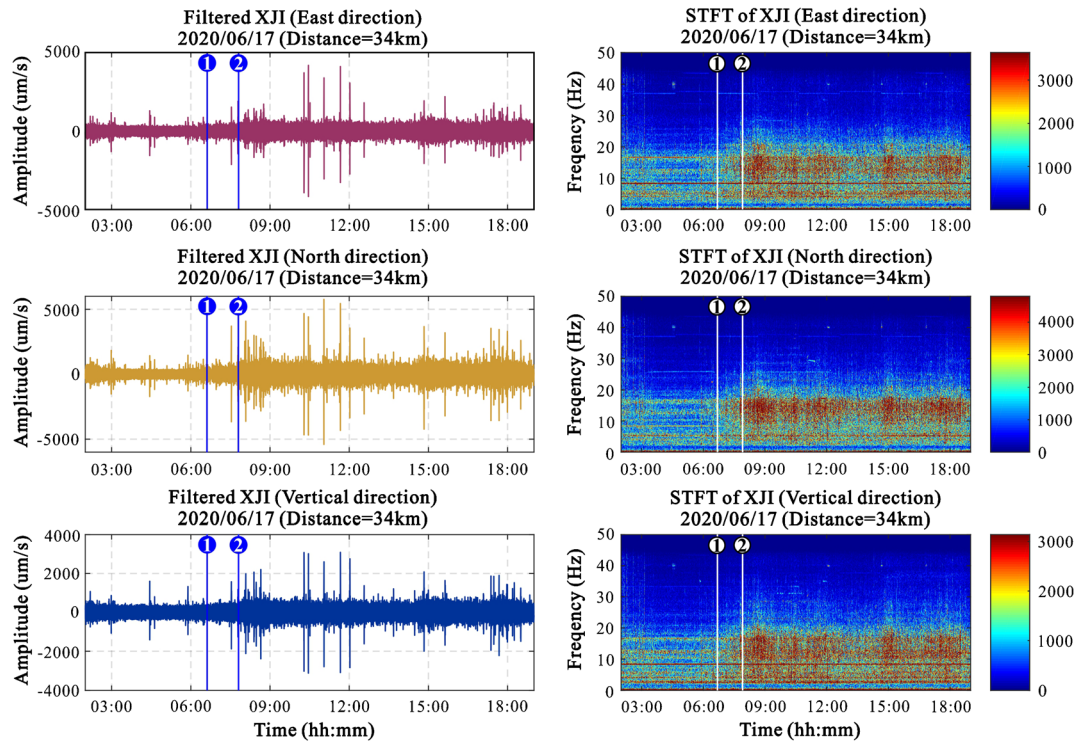


Fig. 8 Signal characteristics of the dammed lake-outbreak flood. This signal is characterized by its frequency bandwidth and high energy. ① Initial large-scale outbreak moment of the dammed lake. ② Second large-scale outbreak moment

Initiation-collapse-stabilization process of the landslide

The dammed lake subsequently naturally collapsed and the remaining dammed body narrowed the channel, causing the flood water to erode the front slope of the ancient landslide body on the left bank. This caused loose deposits at the front edge of the landslide to continuously slide down, and after many small landslides, a surface of ~60 m had formed. This disrupted the balance of the entire ancient landslide body. The ancient landslide above the surface began to destabilize and entered into the landslide initiation stage, which mainly manifested as traction on the surface. The ancient landslide above the surface was gradually activated and slowly began to slide downward (see landslide zone I in Fig. 10). The sliding scale of landslide zone I was relatively small and showed strengthening to weakening characteristics, similar to a spindle.

The collapse stage is characterized by continuous landslides. Four larger landslides can be identified from the vertical seismic curve. The North and East directions of the seismic signal exhibit strong amplitude characteristics due to the interference of the lateral movement of the landslide body in the valley, and the boundaries of each landslide event cannot be clearly identified. The landslide surface of zone II is slightly steeper than that of zone I. The vertical component spectrum of the seismic signal at this stage is wider than that of the initiation stage. The time-frequency characteristics of the collapse stage include a frequency range and high energy. The sliding characteristics of landslide zone II corresponding to the collapse stage are consistent; the signal frequency ranges of the two components in the horizontal direction of the collapse stage are both slightly higher and stronger than those in the initiation stage.

Upon completion of the zone II sliding, zone III gradually entered the collapse stage. The slope of zone III was lower than that of zones I and II, and the generated energy of the vertical component of the signal is relatively weak, which makes it difficult to identify at this stage. In contrast, the north-south component can be relatively easily identified. In the time spectrum, the vertical component reflects the frequency characteristics of the background noise. In the time spectrum of the east-west component and the north-south component, a band-shaped energy cluster can be relatively clearly identified, which corresponds to the maximum value of the time-domain curve.

Hazard chain interpretation

Surface runoff caused by continuous heavy rainfall gathered in Meilonggou and formed water flow, which loosened sediments at the bottom of Meilonggou Gully and weathered rock layers on the gully walls and gradually evolved into a low-density debris flow and ultimately a high-density debris flow. The debris flow eventually stopped due to unloading at the gentle slope of the mouth of Meilonggou (right bank of the Xiaojinchuan River). The duration of the entire debris flow was about 30 min (2:50–3:20, June 17, 2020) (Fig. 11). Approximately 240,000 m³ of debris flow washed out and 110,000 m³ was deposited at the mouth of the gully. Among them, about 130,000 m³ entered the Xiaojinchuan River and deposited, forming a landslide dam around 200 m long and 50 to 100 m wide.

The landslide dam was mainly composed of siliceous rock, slate, sandstone crushed stone, and sandy soil, with poor sorting. The height and stability of the landslide dam gradually decreased from the right bank to the left bank. This feature allowed the

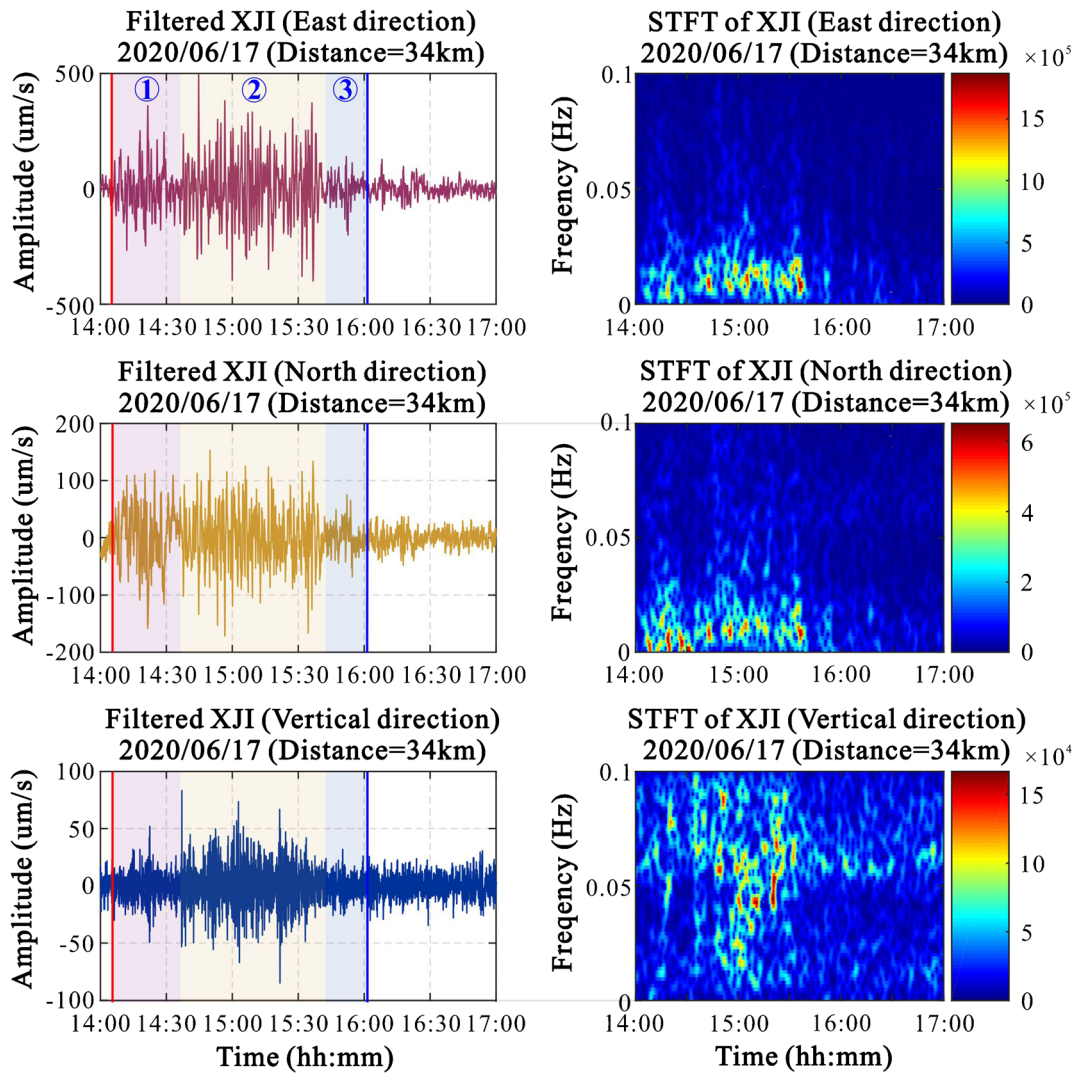


Fig. 9 Seismic time-domain curve and time-frequency spectrum characteristic curve of the Aniangzhai landslide: ① initiation stage; ② collapse stage; and ③ gradual stability stage. The red and blue lines represent the start and end times of the landslide, respectively

dammed lake to initiate natural flood discharge from the left bank after the water depth reached a certain level (6:37 on June 17). Continuous heavy rainfall and upstream erosion of the turbulent water flow eroded the landslide dam, which further increased the natural outbreak flow, and entered the large-scale flood release stage (7:47 on June 17). The XJI seismic station recorded the continuous increase in water flow during this period (Fig. 11). After approximately 5.5 hours of flood discharge, the dammed lake gradually entered a stable state and the discharge flow decreased, showing a time-frequency characteristic similar to background noise in the time-frequency domain (Fig. 11).

While the continuous heavy rainfall and turbulent water flow upstream eroded the landslide dam, the relatively loose slope toe of the Aniangzhai ancient landslide on the left bank was washed away, which caused the lower part of landslide zone I (Fig. 10) to gradually collapse and form a steep slope approximately 60 m high. The formation of the surface disrupted the original landslide zone I equilibrium state (Fig. 10). Under the action of gravity, the slope above the surface began to carry out a larger

scale collapse (14:10, June 17). The entire landslide area destabilized because of the collapse of the northernmost side and began to enter a state of gradual landslides from north to south. The entire landslide state lasted for about 2 hours and was characterized by multiple consecutive sliding events from north to south. The main sliding occurred in the second stage, corresponding to landslide zone II. The continuous multiple sliding events led to 1.2 million m² of an ancient landslide front (zones I–III). The slope deposits of the landslides entered the river and accumulated on the front edge of the dam, hindering natural flood discharge and increasing the scale of the dammed lake. However, because the landslide body was loose gravel and clay, the dam caused by the body slumping stability was low and prone to natural failure, thus resulting in flood signals of failure. At the same time, because of continuous landslides, new landslide dams formed and natural failures occurred again in the dam. Such reciprocation constitutes the characteristics of a dammed lake in the landslide stage (Fig. 12). During this period of time, the seismic signal shows relatively clear characteristics in

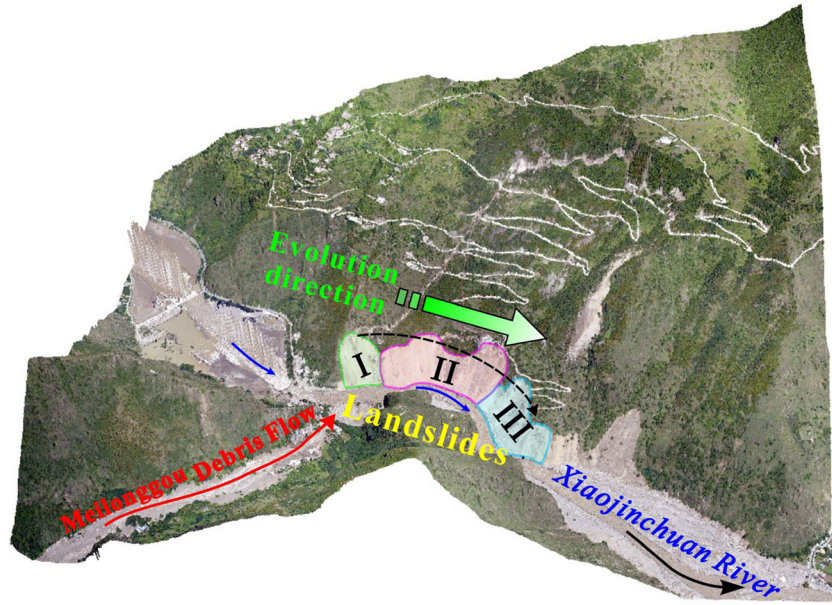


Fig. 10 Schematic diagram of the evolution process of the landslide zone of the Aniangzhai landslide

the time-frequency spectrum, namely, characteristics of a gradual enhancement of the time-frequency spectrum energy cluster and time-domain signal. Upon completion of the Aniangzhai landslide, the dammed lake entered a large-scale flood discharge

stage (Fig. 11). The Aniangzhai landslide caused the entire ancient landslide to be revived in an area of about 6 million m³ and 0.62 km² on the front edge of the ancient landslide (zones I–III). Some secondary landslides remain, which may collapse again.

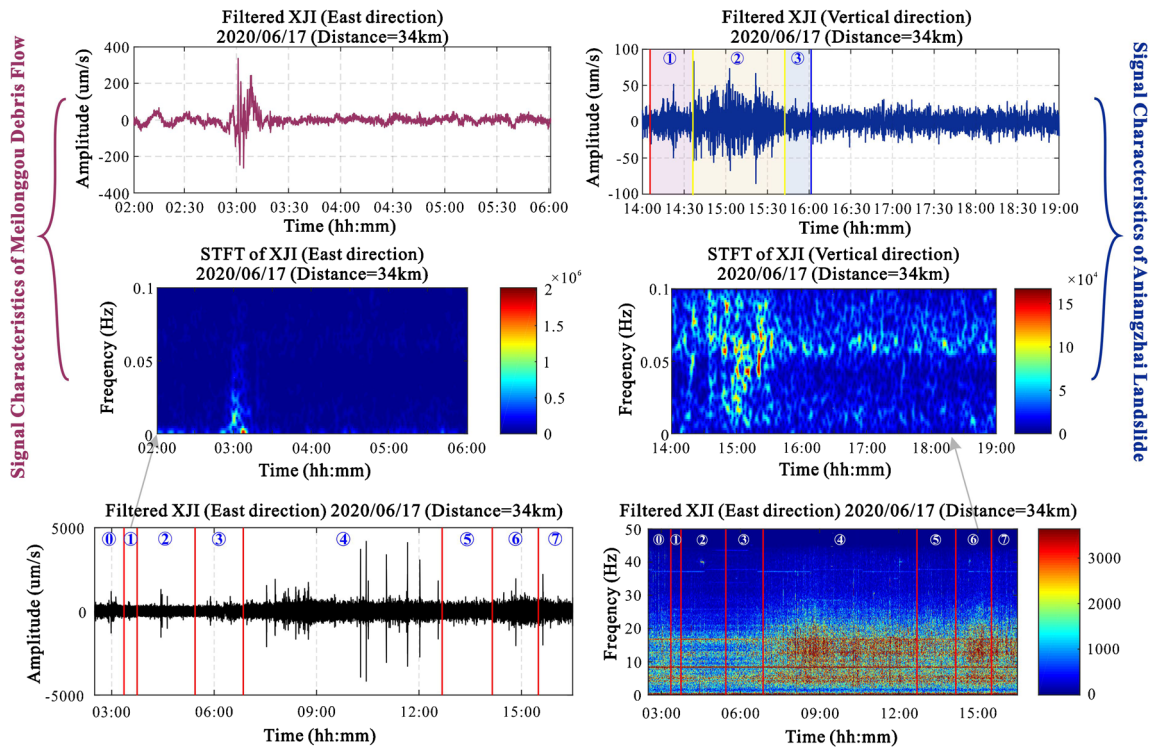


Fig. 11 Time-domain and time-frequency domain signal curve timing diagrams of the complete dammed lake hazard chain process: (0) before the hazard occurs; (1) debris flow hazard stage, corresponding to the initiation, evolution, and deposition process of the debris flow in Meilonggou; (2) dammed lake stage, which is mainly the process by which water levels increase in the dammed lake; (3) growth stage of the dammed lake; (4) dammed lake bursting stage; (5) flood discharge stabilization stage; (6) Aniangzhai landslide stage, which is accompanied by the secondary formation of a dammed lake alternating with failure; and (7) second failure stage of the landslide dammed lake, which starts with the large-scale failure of the dam caused by the landslide

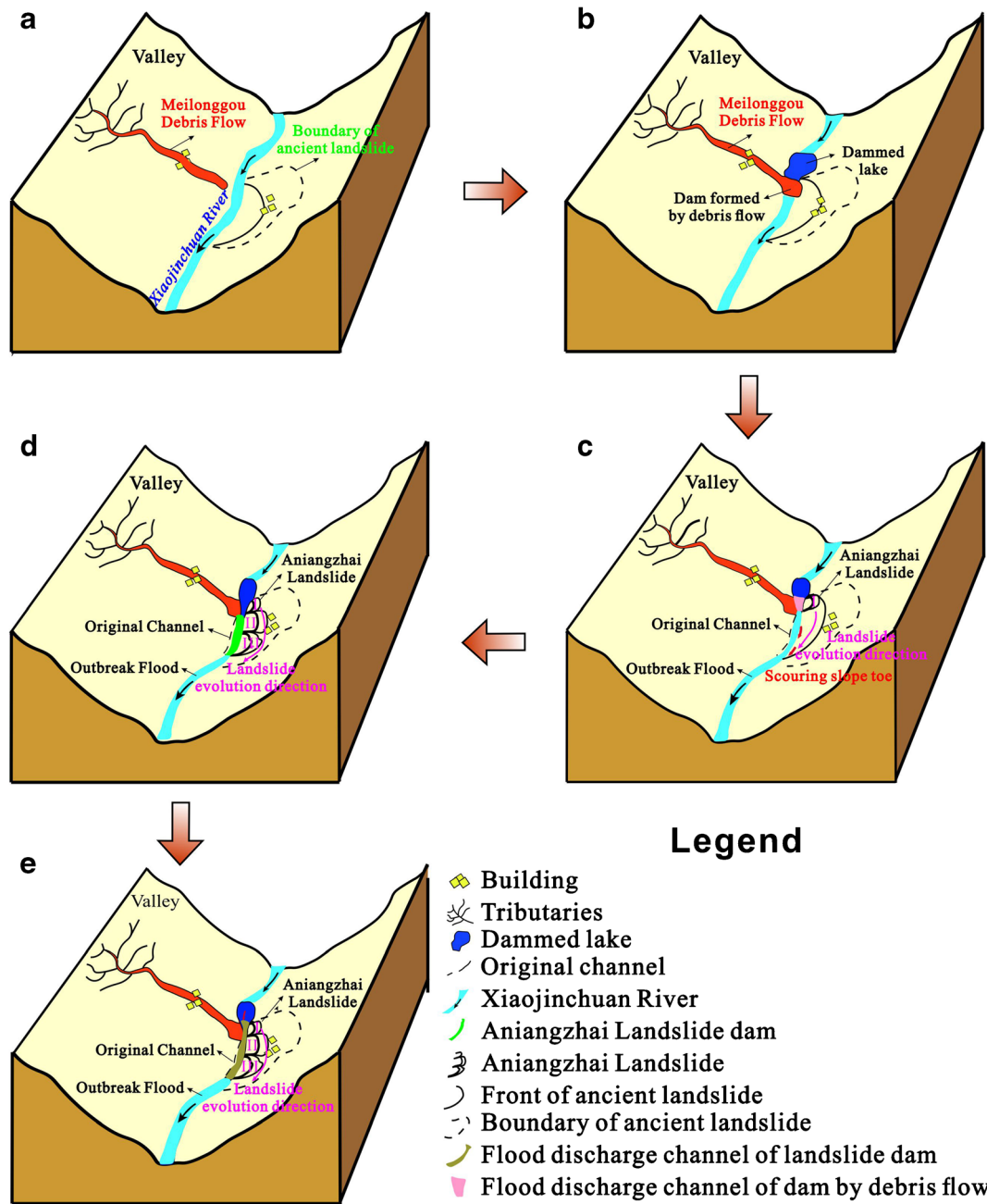


Fig. 12 Mode diagram of the complete hazard chain of the dammed lake: a schematic diagram of the formation process of the Meilonggou debris flow; b schematic diagram of the process by which the debris flow blocks the river to form a dammed lake; c outbreak of the dammed lake and the downstream ancient landslide is swept away by the flood; d schematic diagram of the collapse process of the Aniangzhai landslide to form a dammed lake; and e flood discharge after the outbreak of the dammed lake formed by the Aniangzhai landslide blocking the Xiaojinchuan River

Conclusions and discussions

This paper reports the formation and breach of the Danba debris flow dam on the Xiaojinchuan River in 2020; a comprehensive interpretation of the hazard chain was achieved using developed weak-signal processing by a band-pass filter, empirical mode decomposition, and short-time Fourier transform. The following conclusions were reached:

1. The Meilonggou debris flow was a valley-type debris flow caused by heavy rainfall and stimulated the entire chain of dammed lake hazards, dammed lake-outbreak, and the Aniangzhai landslide. The continuous rainfall in June increased groundwater content and reduced the stability of loose sediments in the study area. On June 17, a short period of heavy rainfall formed surface runoff and formed floods in Meilonggou Gully.

The floods washed away loose sediments in the channels and weathered metamorphic rock bedrock on the channel walls, gradually forming debris flows. The debris flow unloaded at the end of the Meilonggou Gully (right bank of the Xiaojinchuan River) and deposited, which blocked the Xiaojinchuan River. After the dammed lake-outbreak, the flood washed and eroded the foot of an ancient landslide on the left bank of the Xiaojinchuan River, which caused the ancient landslide to become unstable and activated.

2. *This study establishes a set of identification procedures for weak seismic signals of geological hazards, which can help to identify geohazard signals.* The scale of the debris flow and landslide was relatively small and their seismic signals show characteristics of low frequency and weak energy. The signals recorded by the seismic stations near the hazard were analyzed and processed according to a set of weak and low-frequency seismic signal processing procedures. Combining the on-site geological survey and signal characteristics, the weak debris flow, landslide, and flood discharge signals were successfully identified. The seismic data from the geological hazards were affected by the scale, propagation distance, and lithology of the hazard, and received signals are characterized by weak energy, low frequency, and low signal-to-noise ratio.

3. *Joint analysis of seismic signals and post-hazard surveys enabled the interpretation of the Aniangzhai landslide process and indicated that the Aniangzhai landslide was characterized by the continuous sliding of multiple small landslides from north to south.* Combined with the landslide seismic signal, multiple bell-shaped signal features and multiple signals constituted a relatively complete cone-shaped feature. Combined with the landslide volume and the slope of the landslide surface, it was determined that the landslide consisted of multiple continuous small landslides in the entire process of slow sliding–severe sliding–slow sliding–becoming static. This divided the Aniangzhai landslide into three stages that correspond to a landslide zone.

4. *The entire hazard process was interpreted based on the seismic signals, including the occurrence time of each hazard, overlapping relationships, and causes, which provides a theoretical basis for follow-up post-hazard emergency assessment and rescue.* Through analysis of the signals related to the hazard chain recorded by the XJI station, the time sequence of the hazard chain was determined: Meilonggou Gully debris flow–first outbreak of the dammed lake–end of flood discharge–Aniangzhai landslide–landslide dammed lake–second outbreak of the dammed lake. On this basis, the cause and effect of this Danba dammed lake hazard chain were clarified. The methods proposed here can be used to identify hazards in areas with frequent debris flows and ancient landslides or landslide-prone bodies to reduce losses of life and property.

Acknowledgments

This study was financially supported by the Second Tibetan Plateau Scientific Expedition and Research Program (STEP) (No. 2019QZKK0906), the National Natural Science Foundation of China (No. 41941019, 42077238, and 41901008), and the Fundamental Research Funds for the Project of Science and Technology

Department of Sichuan Province (No. 2020YFH0085). This work was also financially supported by the China Scholarship Council. We thank Esther Posner, PhD, and Sara J. Mason, MSc, from Liwen Bianji, Edanz Editing China, for editing the English text of drafts of this manuscript.

References

- Amann F, Kos A, Phillips M, Kenner R (2018) The Piz Cengalo Bergsturz and subsequent debris flows. EGU General Assembly Conference Abstracts 20:14700
- Arattano M, Abancó C, Coviello V, Hürlimann M (2014) Processing the ground vibration signal produced by debris flows: the methods of amplitude and impulses compared. *Comput Geosci* 73:17–27
- Bai YJ, Wang YS, Ge H, Tie YB (2020) Slope structures and formation of rock–soil aggregate landslides in deeply incised valleys. *J Mt Sci* 17(2):316–328
- Begam S, Sen D, Dey S (2018) Moraine dam breach and glacial lake outburst flood generation by physical and numerical models. *J Hydrol* 563:694–710
- Brodsky EE, Gordeev E, Kanamori H (2003) Landslide basal friction as measured by seismic waves. *Geophys Res Lett* 30(24):2236. <https://doi.org/10.1029/2003GL018485>
- Carlo TS, Filippo C, Nicola C (2015) Geomorphological investigations on landslide dams. *Geoenvironmental Disasters* 2(1):21. <https://doi.org/10.1186/s40677-015-0030-9>
- Chen C, Zhang L, Xiao T, He J (2020) Barrier lake bursting and flood routing in the Yarlung Tsangpo Grand Canyon in October 2018. *J Hydrol* 583:124603
- Costa JE, Schuster RL (1988) The formation and failure of natural dams. *Geol Soc Am Bull* 100(7):1054–1068. [https://doi.org/10.1130/0016-7606\(1988\)100<1054:TFAFON>2.3.CO;2](https://doi.org/10.1130/0016-7606(1988)100<1054:TFAFON>2.3.CO;2)
- Cui P, Zhou GGD, Zhu XH, Zhang JQ (2003) Scale amplification of natural debris flows caused by cascading landslide dam failures. *Geomorphology* 182:173–189
- Cui P, Zhu Y, Han Y, Chen X, Zhuang J (2009) The 12 May Wenchuan earthquake-induced landslide lakes: distribution and preliminary risk evaluation. *Landslides* 6(3):209–223. <https://doi.org/10.1007/s10346-009-0160-9>
- Cui P, Zhou GGD, Zhu XH, Zhang JQ (2013) Scale amplification of natural debris flows caused by cascading landslide dam failures. *Geomorphology* 182:173–189. <https://doi.org/10.1016/j.geomorph.2012.11.009>
- Cui YF, Cheng D, Choi CE, Jin W, Lei Y, Kargel JS (2019) The cost of rapid and haphazard urbanization: lessons learned from the Freetown landslide disaster. *Landslides* 16(6):1167–1176. <https://doi.org/10.1007/s10346-019-01167-x>
- Dal Sasso SF, Sole A, Pascale S, Sdao F, Bateman Pinzón A, Medina V (2014) Assessment methodology for the prediction of landslide dam hazard. *Nat Hazards Earth Syst Sci* 14(3):557–567. <https://doi.org/10.5194/nhessd-1-5663-2013>
- Dammeier F, Moore JR, Haslinger F, Loew S (2011) Characterization of alpine rockslides using statistical analysis of seismic signals. *J Geophys Res* 127(3–4):166–178. <https://doi.org/10.1029/2011JF002037>
- Dammeier F, Guilhem A, Moore JR, Haslinger F, Loew S (2015) Moment tensor analysis of rockslide seismic signals. *Bull Seismol Soc Am* 105(6):3001–3014. <https://doi.org/10.1785/0120150094>
- Ding MT, Tang C, Miao C (2020) Response analysis of valley settlements to the evolution of debris flow fans under different topographic conditions: a case study of the upper reaches of Min River, China. *Bull Eng Geol Environ* 79(3):1639–1650. <https://doi.org/10.1007/s10064-019-01641-9>
- Dong J, Liao MS, Xu Q, Zhang L, Tang MG, Gong JY (2018) Detection and displacement characterization of landslides using multi-temporal satellite SAR interferometry: A case study of Danba County in the Dadu River Basin. *Eng Geol* 240:95–109
- Ermini L, Casagli N (2010) Prediction of the behaviour of landslide dams using a geomorphological dimensionless index. *Earth Surf Process Landf* 28(1):31–47. <https://doi.org/10.1002/esp.424>
- Fan XM, Van Westen CJ, Xu Q, Gorum T, Dai F (2012) Analysis of landslide dams induced by the 2008 Wenchuan earthquake. *J Asian Earth Sci* 57:25–37. <https://doi.org/10.1016/j.jseas.2012.06.002>
- Fan XM, Rossiter DG, Van Westen CJ, Xu Q, Görüm T (2014) Empirical prediction of coseismic landslide dam formation. *Earth Surf Process Landf* 39(14):1913–1926. <https://doi.org/10.1002/esp.3585>

- Feng ZY (2011) The seismic signatures of the 2009 Shiaolin landslide in Taiwan. *Nat Hazards Earth Syst Sci* 11(5):1559–1569. <https://doi.org/10.5194/nhess-11-1559-2011>
- Feng ZY (2012) The seismic signatures of the surge wave from the 2009 Xiaolin landslide-dam breach in Taiwan. *Hydrol Process* 26(9):1342–1351. <https://doi.org/10.1002/hyp.8239>
- Feng ZY, Lo CM, Lin QF (2017) The characteristics of the seismic signals induced by landslides using a coupling of discrete element and finite difference methods. *Landslides* 14(2):661–674. <https://doi.org/10.1007/s10346-016-0714-6>
- Feng ZY, Huang HY, Chen SC (2020) Analysis of the characteristics of seismic and acoustic signals produced by a dam failure and slope erosion test. *Landslides* 17(7):1605–1618. <https://doi.org/10.1007/s10346-020-01390-x>
- Helmstetter A, Garambois S (2010) Seismic monitoring of S echillienne rockslide (French Alps): Analysis of seismic signals and their correlation with rainfalls. *J Geophys Res* 115(F3):03016. <https://doi.org/10.1029/2009JF001532>
- Hibert C, Ekstr om G, Stark CP (2014) Dynamics of the Bingham Canyon Mine landslides from seismic signal analysis. *Geophys Res Lett* 41(13):4535–4541. <https://doi.org/10.1002/2014GL060592>
- Hu KH, Wei FQ, Li Y (2011) Real-time measurement and preliminary analysis of debris-flow impact force at Jiangjia Ravine, China. *Earth Surf Process Landf* 36(9):1268–1278
- Huang NE, Wu Z (2008) A review on Hilbert-Huang transform: method and its applications to geophysical studies. *Rev Geophys* 46(2). <https://doi.org/10.1029/2007RG000228>
- Huang CJ, Yin HY, Chen CY, Yeh CH, Wang CL (2007) Ground vibrations produced by rock motions and debris flows. *J Geophys Res Earth Surf* 112(F2):F02014. <https://doi.org/10.1029/2005JF000437>
- Huang CJ, Yeh CH, Chen CY, Chang ST (2008) Ground vibrations and airborne sounds generated by motion of rock in a river bed. *Nat Hazards Earth Syst Sci* 8(5):1139–1147. <https://doi.org/10.5194/nhess-8-1139-2008>
- Huang X, Li Z, Fan J, Yu D, Xu Q (2020) Frequency Characteristics and Numerical Computation of Seismic Records Generated by a Giant Debris Flow in Zhouqu, Western China. *Pure Appl Geophys* 177(1):347–358
- Huggel C (2009) Recent extreme slope failures in glacial environments: effects of thermal perturbation. *Quat Sci Rev* 28(11–12):1119–1130. <https://doi.org/10.1016/j.quascirev.2008.06.007>
- Kao H, Kan C, Chen R, Chang C, Rosenberger A, Shin T, Leu P, Kuo K, Liang W (2012) Locating, monitoring, and characterizing typhoon-induced landslides with real-time seismic signals. *Landslides* 9(4):557–563
- King J, Loveday I, Schuster RL (1989) The 1985 Bairaman landslide dam and resulting debris flow, Papua New Guinea. *Q J Eng Geol* 22(4):257–270. <https://doi.org/10.1144/GSL.QJEG.1989.022.04.02>
- Kogelnig A, H ubl J, Suri nach E, Vilajosana I, McArdell B (2014) Infrasound produced by debris flow: propagation and frequency content evolution. *Nat Hazards* 70(3):1713–1733
- Lai VH, Tsai VC, Lamb MP, Ulizio TP, Beer AR (2018) The seismic signature of debris flows: Flow mechanics and early warning at Montecito, California. *Geophys Res Lett* 45:5528–5535. <https://doi.org/10.1029/2018GL077683>
- Lei Y, Cui P, Zeng C, Guo YY (2018) An empirical mode decomposition-based signal process method for two-phase debris flow impact. *Landslides* 15(2):297–307. <https://doi.org/10.1007/s10346-017-0864-1>
- Li Z, Huang X, Xu Q, Yu D, Fan J, Qiao X (2017) Dynamics of the Wulong landslide revealed by broadband seismic records. *Earth, Planets and Space* 69(1):1–10. <https://doi.org/10.1186/s40623-017-0610-x>
- Li HB, Qi SC, Yang XG, Li XW, Zhou JW (2020) Geological Survey and Unstable Rock Block Movement Monitoring of a Post-Earthquake High Rock Slope Using Terrestrial Laser Scanning. *Rock Mech Rock Eng* 53:1–15. <https://doi.org/10.1007/s00603-020-02178-0>
- Liu D, Cui Y, Guo J, Yu Z, Chan D, Lei M (2020) Investigating the effects of clay/sand content on depositional mechanisms of submarine debris flows through physical and numerical modeling. *Landslides*. 17:1863–1880. <https://doi.org/10.1007/s10346-020-01387-6>
- Liu ZJ, Qiu HJ, Ma SY, Yang DD, Pei YQ, Du C, Sun HS, Hu S, Zhu YR (2021) Surface displacement and topographic change analysis of the Changhe landslide on September 14, 2019, China. *Landslides*. <https://doi.org/10.1007/s10346-021-01626-4>
- Loew S, Gschwind S, Gischig V, Keller-Signer A, Valent G (2017) Monitoring and early warning of the 2012 Preonzo catastrophic rock slope failure. *Landslides* 14:141–154
- Ma SY, Qiu HJ, Hu S, Yang DD, Liu ZJ (2021) Characteristics and geomorphology change detection analysis of the Jiangdingya landslide on July 12, 2018, China. *Landslides* 18:383–396. <https://doi.org/10.1007/s10346-020-01530-3>
- Nian TK, Wu H, Chen GQ, Zheng DF, Zhang YJ, Li DY (2018) Research progress on stability evaluation method and disaster chain effect of landslide dam. *Chin J Rock Mech Eng* 37(8):1796–1812. (in Chinese). <https://doi.org/10.13722/j.cnki.jrme.2017.1655>
- Niu ZP, Xu WL, Li NW, Xue Y, Chen HY (2012) Experimental investigation of the failure of cascade landslide dams. *Journal of Hydrodynamics. Series B* 24(3):430–441. [https://doi.org/10.1016/S1001-6058\(11\)60264-3](https://doi.org/10.1016/S1001-6058(11)60264-3)
- Richter HH, Trigg KA (2008) Case history of the June 1, 2005 Bluebird Canyon landslide in Laguna Beach, California. *GeoCongress 2008: Geosustainability and Geohazard Mitigation*:433–440 10.1061/40971(310)54
- Safraan EB, O'Connor JE, Ely LL, House PK, Grant G, Harrity K, Croall K, Jones E (2015) Plugs or flood-makers? The unstable landslide dams of eastern Oregon. *Geomorphology* 248:237–251
- Sassa K, Fukuoka H, Wang F, Wang G (2005) Dynamic properties of earthquake-induced large-scale rapid landslides within past landslide masses. *Landslides* 2(2):125–134
- Schimmel A, H ubl J (2016) Automatic detection of debris flows and debris floods based on a combination of infrasound and seismic signals. *Landslides* 13(5):1181–1196. <https://doi.org/10.1007/s10346-015-0640-z>
- Sheng MH, Chu RS, Wei ZG, Bao F, Guo AZ (2018) Study of microseismicity caused by Xishancun Landslide deformation in Li country, Sichuan Province. *Chin J Geophys* 61(01):171–182. (in Chinese). <https://doi.org/10.6038/cjg2018L0367>
- Shi XS, Zhao J (2020) Practical estimation of compression behavior of clayey/silty sands using equivalent void-ratio concept. *J Geotech Geoenviron* 146(6):04020046
- Shi ZM, Guan SG, Peng M, Zhang LM, Zhu Y, Cai QP (2015) Cascading breaching of the Tangjiashan landslide dam and two smaller downstream landslide dams. *Eng Geol* 193:445–458. <https://doi.org/10.1016/j.enggeo.2015.05.021>
- Shi XS, Zhao J, Gao Y (2021) A homogenization-based state-dependent model for gap-graded granular materials with fine-dominated structure. *Int J Numer Anal Methods Geomech*. <https://doi.org/10.1002/nag.3189>
- Tsai VC, Minchew B, Lamb MP, Ampuero JP (2012) A physical model for seismic noise generation from sediment transport in rivers. *Geophys Res Lett* 39(2):189–202. <https://doi.org/10.1029/2011GL050255>
- Tsou CY, Feng ZY, Chigira M (2011) Catastrophic landslide induced by typhoon Morakot, Shiaolin, Taiwan. *Geomorphology* 127(3–4):166–178. <https://doi.org/10.1016/j.geomorph.2010.12.013>
- Wang GQ (2013) Millimeter-accuracy GPS landslide monitoring using Precise Point Positioning with Single Receiver Phase Ambiguity (PPP-SRPA) resolution: a case study in Puerto Rico. *Journal of Geodetic Science (Online)* 3(1):22–31. <https://doi.org/10.2478/jogs-2013-0001>
- Wang B, Zhang T, Zhou Q, Wu C, Chen YL, Wu P (2015) A case study of the Tangjiashan landslide dam-break. *J Hydrodyn* 27(2):223–233. [https://doi.org/10.1016/S1001-6058\(15\)60476-0](https://doi.org/10.1016/S1001-6058(15)60476-0)
- Wang W, Yang J, Wang Y (2020) Dynamic processes of 2018 Sedongpu landslide in Namcha Barwa–Gyala Peri massif revealed by broadband seismic records. *Landslides* 17(2):409–418. <https://doi.org/10.1007/s10346-019-01315-3>
- Wei K, Ouyang C, Duan H, Li Y, Chen M, Ma J, An H, Zhou S (2020) Reflections on the Catastrophic 2020 Yangtze River Basin Flooding in Southern China. *The Innovation* 1(2):100038
- Xu Q, Fan XM, Zhang RQ, Westen CV (2009) Landslide dams triggered by the Wenchuan Earthquake, Sichuan Province, south west China. *Bull Eng Geol Environ* 68(3):373–386
- Yamada M, Matsushi Y, Chigira M, Mori J (2012) Seismic recordings of landslides caused by Typhoon Talas (2011), Japan. *Geophys Res Lett* 39(13):L13301. <https://doi.org/10.1029/2012GL052174>
- Yamada M, Kumagai H, Matsushi Y, Matsuzawa T (2013) Dynamic landslide processes revealed by broadband seismic records. *Geophys Res Lett* 40(12):2998–3002. <https://doi.org/10.1002/grl.50437>
- Yan Y, Cui P, Chen SC, Chen XQ, Chen HY, Chien YL (2017) Characteristics and interpretation of the seismic signal of a field-scale landslide dam failure experiment. *J Mt Sci* 14(2):219–236
- Yan Y, Cui YF, Guo J, Hu S, Wang ZA, Yin SY (2020a) Landslide reconstruction using seismic signal characteristics and numerical simulations: Case study of the 2017 “6.24” Xinmo landslide. *Engineering Geology*:105582.
- Yan Y, Cui YF, Tian X, Hu S, Guo J, Wang Z, Yin SY, Liao LF (2020b) Seismic signal recognition and interpretation of the 2019 “7.23” Shuicheng landslide by seismogram stations. *Landslides* 17(5):1191–1206
- Zhang Z, He SM, Liu W, Liang H, Yan SX, Deng Y, Bai XQ, Chen Z (2019) Source characteristics and dynamics of the October 2018 Baige landslide revealed by broadband seismograms. *Landslides* 16(4):777–785
- Zhou GGD, Cui P, Chen HY, Zhu XH, Tang JB, Sun QC (2013) Experimental study on cascading landslide dam failures by upstream flows. *Landslides* 10(5):633–643. <https://doi.org/10.1007/s10346-012-0352-6>
- Zhou M, Zhou GGD, Cui KFE, Song D, Lu X (2019) Influence of inflow discharge and bed erodibility on outburst flood of landslide dam. *J Mt Sci* 16(4):778–792

Zhu X, Xu Q, Zhao Z, Li T (2016) Low frequency acoustic signals associated with rock falls, thunderstorms, and wind turbulences in field environment. *Appl Acoust* 112:131–139. <https://doi.org/10.1016/j.apacoust.2016.05.021>

Y. Yan

Key Laboratory of High-Speed Railway Engineering, MOE/School of Civil Engineering, Southwest Jiaotong University, Chengdu, 610031, China

Y. Cui · L. Zhang

State Key Laboratory of Hydroscience and Engineering, Tsinghua University, Beijing, 100084, China
Email: yifeicui@mail.tsinghua.edu.cn

Y. Yan

Institute of Geographic Sciences and Natural Resources Research, Chinese Academy of Sciences, Beijing, 100101, China

D. Liu

Key Laboratory of Mountain Surface Process and Hazards/Institute of Mountain Hazards and Environment,

Chinese Academy of Sciences, Chengdu, 610041, China

H. Tang

Section 4.7: Earth Surface Process Modelling, German Research Centre for Geosciences (GFZ), Potsdam, Germany

Y. Li

Sichuan Institute of Land and Space Ecological Restoration and Geological Hazard Prevention, Chengdu, 610081, China

X. Tian

Institute of Geophysics, China Earthquake Administration, Beijing, 100081, China

S. Hu

College of Urban and Environmental Sciences, Northwest University, Xi'an, 710127, China